RSC Advances

ROYAL SOCIETY OF CHEMISTRY

www.rsc.org/advances

Journal Name

ARTICLE

Controllable Synthesis of In_2O_3 Octodecahedra Exposing {110} Facets with Enhanced Gas Sensing Performance

Received 00th January 20xx,
Accepted 00th January 20xx

DOI: 10.1039/x0xx00000x

www.rsc.org/

Jijiang Liu,[ab] Gang Chen,*[a,] Yaoguang Yu,*[a,] Yalin Wu,[b] Mingjun Zhou,[b] Hongquan Zhang,[c] Chade Lv,[a] Yi Zheng,[a] Fang He[a]

In_2O_3 octodecahedra have been successfully prepared by annealing the 18-facet $In(OH)_3$ precursor. The as-prepared In_2O_3 polyhedra inherit the morphology of the $In(OH)_3$ precursor and expose twelve {110} and six {100} facets. Gas sensing tests show that octodecahedron-based In_2O_3 sensor exhibits a sensitivity of 610 to 1000 ppm ethanol, which is 2.3-fold and 5.5-fold enhancement compared with cube- and particle-based sensor, respectively. The XPS results demonstrate that the {110} and {100} facets of In_2O_3 octodecahedra provided more oxygen vacancies than either the cubes exposing only {100} facets or the irregular particles. More oxygen vacancies would contribute to the enhancement of gas sensing performance. The crystal facet analysis of In_2O_3 octodecahedra show that high energy {110} facets could be easier to form oxygen vacancy than that of {100} facets, which could be the main reason for high gas sensing property. This finding will open a door to the design of high performance gas sensor, and the results are also beneficial to other fields such as energy conversion, environmental protection.

Introduction

The physical and chemical properties of crystals are related to not only the large proportion of surface atoms but also the crystallographic structure of the particle surface. The percentage of atoms at the particle surface is determined by the size of the particle. On the other hand, the crystallographic structure of the particle surface relies on the particle shape.[1-3] To maximize their properties, both the size and the shape of crystals are critical factors that should be controlled.[4] In_2O_3 is widely studied because of its feasible fabrication, low cost and excellent gas sensing properties towards different oxidizing and reducing gases.[5-8] There has been a great deal of effort to investigate the effect of In_2O_3 particle size on their gas sensing properties.[9-11] Although the decrease of the grain size is one of the main approaches used for the improvement of sensor response of metal oxide gas sensors, the smaller primary particles are easy to grow and aggregate into bigger secondary particles during high temperature treatment. The aggregated particles would decrease its surface area and porosity, which is the main reason for the deterioration of the gas sensing performance.[12-14]

The surface effects are shape-dependent since the relative number of surface atoms depends on the particle shape. The gas sensing ability of metal oxide semiconductors is theoretically very sensitive to the crystal facets of the sensing materials with different shape.[15] Octahedral SnO_2 nanoparticles with exposed {221} facets show superior gas sensing performance to different gases compared with elongated-octahedral and lance-shaped SnO_2.[16, 17] The sensing properties of ZnO nanodisks and nanowhiskers are found to be superior to that of nanowires and nanostars. The enhancement in sensitivity is attributed to the surface polarities of the different structures.[18, 19] $CdIn_2O_4$ with octahedral shape reveals excellent ethanol gas response.[20] Polyhedral $ZnSnO_3$ microcrystal with controlled exposed facets exhibits different sensitivity to the species and concentrations of the analyte gases.[21] Due to distinguishing ability of In_2O_3, gas sensing application of this material has received much attention. Researchers have focused tremendous efforts on developing In_2O_3-based gas sensors to improve sensitivity, selectivity, stability and response/recovery times.[22] Although many micro/nano-sized In_2O_3 materials with different morphologies have been prepared including zero-dimensional,[23, 24] one-dimensional,[25-28] two-dimensional,[29, 30] and three-dimensional In_2O_3 materials,[31-33] few research is focused on the shape effect of In_2O_3 on gas sensing performance as it is still a challenge for controllable synthesis of the particle shape.[34, 35] For the *bcc* In_2O_3, the sequence of surface energy (γ) for low index crystallographic facets is γ {111} < γ {001} < γ {110}.[36] Recently, In_2O_3 polyhedral nanostructures exposing {100} and {111} facets have been

[a] *Department of Chemistry, Harbin Institute of Technology, Harbin 150001, P. R. China*
[b] *The 49th Research Institute, China Electronic Technology Group Corporation, Harbin 150001, P. R. China*
[c] *School of Automation, Harbin Engineering of University, Harbin 150001, P. R. China*
† E-mail: gchen@hit.edu.cn; (G. Chen); ygyu@hit.edu.cn (Y. G. Yu). Fax: +86-451-86403117; Tel: +86-451-86403117.
Electronic Supplementary Information (ESI) available: [SEM images of $In(OH)_3$ and In_2O_3: cubes and particles (Fig. S1); XRD patterns of the In_2O_3 cubes and particles (Fig. S2).]See DOI: 10.1039/x0xx00000x

prepared, which show excellent photocatalytic property.[37, 38] In_2O_3 polyhedron enclosed by {110} facet and its gas sensing performance have not been reported. In the present work, the relationship between {110} facet and the gas sensing performance of In_2O_3 octodecahedra is firstly investigated. This finding would provide a new insight into the influence of the surface atom arrangement on the gas sensing performance.

Herein, we report a facile method for the preparation of In_2O_3 octodecahedra by annealing the 18-facet $In(OH)_3$ precursors. The octodecahedral In_2O_3 is enclosed by twelve {110} and six {100} facets. In_2O_3 cubes exposing only {100} facets and irregular In_2O_3 particles are also prepared to compare the gas sensing performance with In_2O_3 octodecahedra. Detailed research of sensing property reveals that the shape of In_2O_3 particle greatly affects the sensor sensitivity. Octodecahedral In_2O_3 shows the best gas sensing properties compared with the cubes and particles counterpart. The experimental and analytic results suggest that the exposed {110} facet is the main reason for the improvement of the gas sensing performance.

Experimental

Synthesis of In_2O_3 Polyhedra, Cubes and Particles

All of the reagents, indium chloride tetrahydrate ($InCl_3 \cdot 4H_2O$, AR), sodium hydroxide (NaOH, A.R) and absolute ethanol were used as received without any further purification. Deionized water was used throughout the experiments.

In a typical synthesis of octodecahedral In_2O_3, $InCl_3 \cdot 4H_2O$ (0.293 g, 1 mmol) were added to ethanol (25 ml) to form a solution A. NaOH (2 g, 50 mmol) was dissolved in mixed deionized water (10 ml) to form a solution B. Under magnetic stirring, solution A was dropped into solution B to form a white solution. The mixing solution was put into a Teflon-lined autoclave of 50 mL capacity. The autoclave was sealed and heated at 200 °C for 24 h. Then, the autoclave was allowed to cool to room temperature naturally. The resulting white products $In(OH)_3$ were centrifuged and rinsed with deionized water and absolute ethanol several times and dried for 4 h at 80 °C before further characterization. For transformation of $In(OH)_3$ to In_2O_3, the products $In(OH)_3$ were put into a corundum crucible with a capacity of 30 ml, kept at 300 °C for 2 h. The final powders are collected for subsequent characterization.

Similarly, In_2O_3 cubes were prepared by reducing the amount of NaOH from 2 g to 0.1 g in the solution B and absolute ethanol was replaced completely by deionized water in the solution A, while other reaction conditions were kept constant. For the synthesis of In_2O_3 particles, the amount of NaOH was reduced from 2 g to 0.1 g. The amount of deionized water in solution B was 5 ml and absolute ethanol was 5 ml, while other reaction conditions were kept constant.

Characterization

X-ray diffraction (XRD) analysis was conducted on a TD-3500 X-ray diffractometer with Cu Kα1 radiation (λ=1.54056Å). Scanning electron microscopy (SEM) images were recorded on a FEI INSPECT S 50 microscope operating at 25 kV. Thermogravimetry-Differential Scanning Calorimetry (TG-DSC) was performed using a Netzsch STA 499 F1 Juptier in flowing Ar gas at a heating rate of $10 \cdot min^{-1}$. Transmission electron microscopy (TEM) and high-resolution transmission electron microscopy (HRTEM) images were obtained by employing a FEI Tecnai G2 S-Twin transmission electron microscope with a field-emission gun operating at 200 kV. The surface areas of the three types of In_2O_3 samples with different shapes were measured by the BET method by measuring nitrogen-adsorption and desorption isotherms on an AUTOSORB-1 Surface Area and Pore Size Analyzer. XPS measurements were performed on a PHI 5700 XPS/ESCA system with a monochromatic Al Kα (1486.6 eV). All binding energies were calibrated to C1s peak at 284.6 eV of the surface adventitious carbon.

Gas Sensor Fabrication and Measurement

The gas sensors were fabricated and measured as follows: The gas sensor was fabricated by coating the slurry of three In_2O_3 powder with different morphology onto the ceramic tube without an additional annealing process. Then an alloy coil through the tube was employed as a heater to control the operating temperature. The electrical contact was made through connecting the four platinum wires on the ceramic tube with the socket by gold paste. Typically, the gas sensors were placed in a chamber and the gas sensing experiments were conducted under a laboratory conditions. The response of the sensor was defined as $S=R_a/R_g$, where R_a and R_g were the resistances of the sensor in the air and target gas, respectively. The response and recovery times are defined as the time taken by the sensor to achieve 90 % of the total resistance change during adsorption and desorption process, respectively.

Results and discussion

Structural and Morphological Characterization

The crystal structure of $In(OH)_3$ was examined by XRD (Fig. 1a). All diffraction peaks in this pattern can be indexed to cubic $In(OH)_3$ (JCPDS No. 76-1464). No impurities, such as InOOH or In_2O_3, are detected, indicating the high purity of the samples. Sharp and strong diffraction peaks suggest the high crystalline quality of the as-prepared products. The intensity ratio of (220) to (200) peak is higher than that in the corresponding standard pattern (JCPDS No. 76-1464), which indicates a high proportion of {110} facets for the obtained 18-facet polyhedra.[39, 40] Fig. 1b shows a typical low-magnification SEM image of $In(OH)_3$ octodecahedra, in which many 18-facet $In(OH)_3$ polyhedra with the size of approximately 0.3 μm-2 μm could be recognized. High-magnification SEM image in the inset of Fig. 1b reveals clearly well-defined facets, sharp edges and vertices of the In_2O_3 octodecahedra. For a *bcc* crystal, Wang et al. declared that octodecahedra are enclosed by different combinations of {110} and {100} facets.[41] $In(OH)_3$ octodecahedra with *bcc* structure are enclosed by 6 squares of {100} top facets and 12

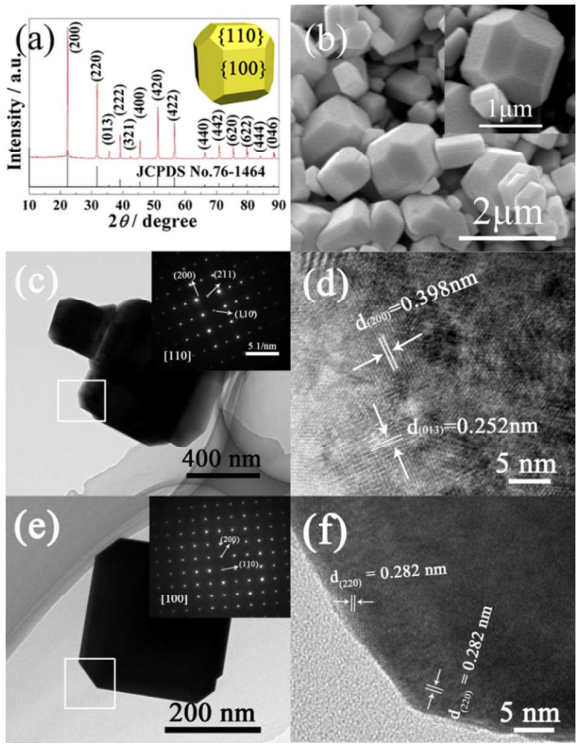

Fig. 1 (a) XRD pattern of 18-facet $In(OH)_3$ precursor and (b) Low-magnified SEM image. (c, e) TEM image and (d, f) HRTEM image of $In(OH)_3$ octodecahedra. Insets in Fig. 1(a), (b), (c) and (e) are three-dimensional model of octodecahedra, corresponding high-magnified SEM image and the SAED patterns along the [110] and [100] zone axis, respectively.

hexagons of {110} side facets. In addition, there are 48 edges and 32 vertices in this octodecahedra. The relation of the numbers of faces (F), edges (E), and vertices (V) follows Euler's rule (V+F-E=2) for a typical convex polyhedron.[42] The structure can be illustrated by the model presented in the inset of Fig. 1a.The detailed description of 18-facet polyhedral characteristics can be found the previous literature.[43, 44] TEM images (Fig. 1c and e) demonstrate the octodecahedral geometry and smooth surfaces of $In(OH)_3$. The SAED patterns (the insets in Fig. 1c and e) indicate the existence of {110} and {100} facets. Furthermore, the HRTEM images (Fig. 1d and 1f) show the different interplanar distances and verify that the polyhedra are single-crystalline.

Phase Transformations of $In(OH)_3$ to In_2O_3

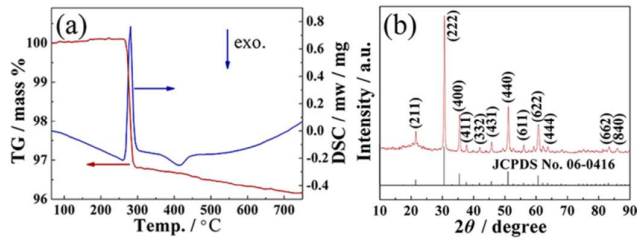

Fig. 2 (a) TG-DSC curves of $In(OH)_3$ octodecahedra and (b) XRD pattern of In_2O_3 octodecahedra.

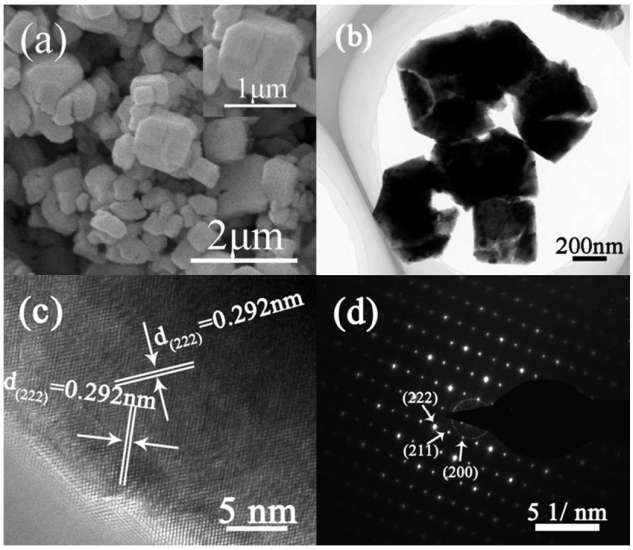

Fig. 3 (a) SEM image and (b) TEM image of In_2O_3 octodecahedra. (c) HRTEM image and (d) SAED pattern of In_2O_3 octodecahedra.

In_2O_3 octodecahedra are obtained by annealing corresponding 18-facet $In(OH)_3$ polyhedra. The phase transformation process of the $In(OH)_3$ sample during calcinations in Ar gas was studied *via* TG-DSC (Fig. 2a). It is observed that the decomposition started at 260 °C and finished at 290 °C in the TG curve of $In(OH)_3$. All the $In(OH)_3$ samples prepared in this work show similar thermogravimetric curves. The TG-DSC curve indicates an endothermic reaction around 280 °C. Fig. 2b shows the XRD pattern of the In_2O_3 product obtained by annealing as-prepared $In(OH)_3$ at 300 °C for 2 h. All of the peaks can be indexed to the pure cubic phase of In_2O_3 (JCPDS No. 06-0416), indicating that InOOH is not formed during the dehydration process of $In(OH)_3$. The $In(OH)_3$ directly converts into cubic phase of In_2O_3 in our experiment at 290 °C. Hence, the annealing temperature is ascertained to be 300 °C in order to obtain pure In_2O_3 products.

Detailed morphological characterization is also carried out to ascertain the structural integrity and morphological change of In_2O_3 polyhedra that occurs under annealing condition. Fig. 3a, b show the corresponding SEM and TEM image of as-prepared In_2O_3 octodecahedra. Although many cracks and irregular pores can be observed on the surface, In_2O_3 polyhedra still retains the octodecahedral shape (Fig. 3a). These phenomena are further demonstrated by TEM (Fig. 3b), which shows that many cracks and pores on the products are generated by the dehydration of precursor $In(OH)_3$ and contribute to the improvement of gas sensing properties. TEM observation reveals that the octodecahedral morphologies of $In(OH)_3$ are maintained after dehydration. HRTEM was employed to further confirm the crystalline structures. The lattice fringes of (222) can be seen in Fig. 3c. The HRTEM image also demonstrates the high crystallinity of In_2O_3 and steps present on the surface. The selected area electron diffraction (SAED) pattern could be indexed to the (222), (211) and (200) planes of the In_2O_3 *bcc* crystal lattice in Fig. 3d. The HRTEM

image and SAED pattern verify that the In_2O_3 octodecahedra are single-crystalline.

Gas Sensing Properties

Gas sensing is a surface phenomenon, which depends on various factors, such as surface area, grain size, structural defects, surface energy etc. To investigate the effects of shape and size on gas sensing performance, In_2O_3 cubes with only {100} facets and irregular particles are also prepared by annealing the corresponding $In(OH)_3$ cubes and particles precursors. A panorama view of the products shows that the In_2O_3 cubes and particles inherit their precursor morphology (Fig. S1). The final products are the pure cubic phase of In_2O_3, as confirmed by the X-ray diffraction patterns (Fig. S2). In gas sensing experiments, ethanol was used as an analyte molecular to investigate gas sensing properties of the In_2O_3 octodecahedra, cubes and particles sensors.

The response of a semiconductor gas sensor is highly sensitive to the operating temperature which may result from the temperature-dependent adsorption–desorption kinetic process and activation energy.[45, 46] Fig. 4a shows the change of sensitivity of three kinds of sensors to 1000 ppm ethanol gas with different operating temperature. Obviously, the sensitivity of each sensor strongly depends on the operating temperature. Each sensor has an optimal operating temperature, at which the sensor exhibits the highest response to ethanol gas. When the operating temperature is 200 °C, the sensor based on In_2O_3 octodecahedra with {110} and {100} facets exhibits the highest response to ethanol gas compared with that based on cubes with only {100} facets and irregular particles. From the SEM in Fig. 3a and Fig. S1, we can clearly observe that In_2O_3 octodecahedra and cubes have bigger grain size than In_2O_3 particles. The results show that the enhanced gas sensing performance of the octodecahedral In_2O_3 is not due to the grain size but the shape and surface structure of the material. The superior sensing properties for In_2O_3 octodecahedra are further supported by the sensor response/recovery time curves (Fig. 4b). The results present the rapid response and recovery time of three kinds of In_2O_3 sensors. It is clear that In_2O_3 octodecahedra have the highest sensitivity. The sensor is very stable at high concentration. The response time of three kinds of sensors is about 1-2 s and recovery time is 15-20 s to 1000 ppm ethanol. The slow recovery time is attributed to low operating temperature, which does not contribute to desorption of reaction products.

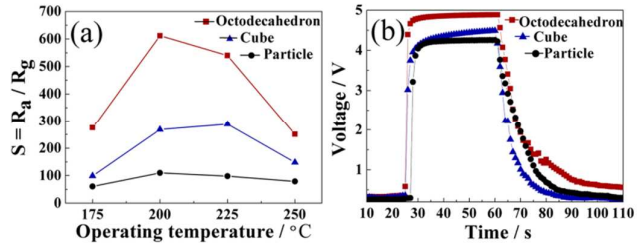

Fig. 4 (a) Gas responses of the three kinds of In_2O_3 sensors to 1000 ppm ethanol as a function of operating temperature. (b) Response and recovery time of the different morphological In_2O_3 to 1000 ppm ethanol at 200 °C.

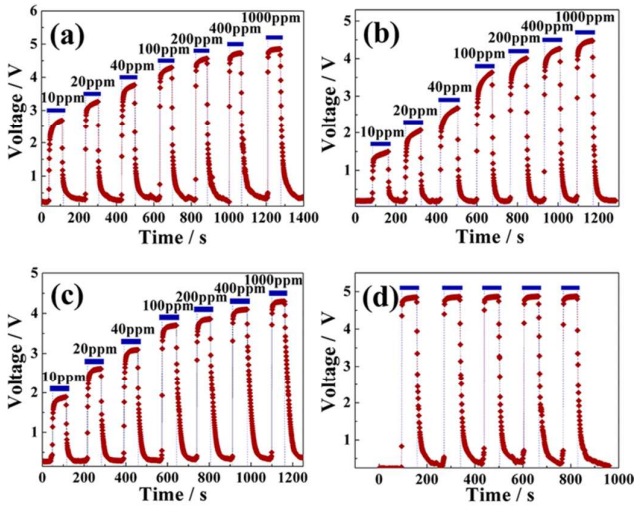

Fig. 5 Response transients of the three kinds of In_2O_3 sensors to different concentration ethanol (a) octodecahedra, (b) cubes and (c) particles. (d) repeated response curve of In_2O_3 octodecahedra sensor to 1000 ppm ethanol.

To illustrate the excellent response of the octodecahedral In_2O_3 sensor, we also compared the response of In_2O_3 octodecahedra sensor with that of In_2O_3 cubes and particles sensor to different concentration ethanol gas. Fig. 5 (a–c) shows the dynamic response curves of three kinds of In_2O_3 sensors to different ethanol concentration range from 10 ppm-1000 ppm at 200 °C. As can be seen, the sensitivities of gas sensors increase rapidly with the enhancement of ethanol concentration. Sensors based on In_2O_3 octodecahedra have high sensitivity at both high and low ethanol concentration. The octodecahedral In_2O_3 sensor has a sensitivity of 26 to ethanol concentration of 10 ppm, while the sensitivity is only 11 for the In_2O_3 cubes and particles sensors. The results indicate that In_2O_3 octodecahedra sensor has lower detection limit than that of In_2O_3 cubes and particles sensors. Fig. 5d shows a series of repeated response of the In_2O_3 octodecahedra sensor to dynamic switches between air and testing gas at 200 °C, which provides more information on three of the most important parameters for a gas sensing device: sensitivity, response/recovery time and reproducibility. The sensor made in the present work has a good reproducibility with relatively minor deviations for five replicate injections.

Gas Sensing Mechanism

The fundamental gas sensing mechanism of metal oxide sensor involves an adsorption–oxidation–desorption process, in which chemisorbed oxygen species play a crucial role. Since electrons are transferred from the crystal bulk to chemisorbed oxygen and result in reactive oxygen species, an electron-depletion layer is formed on the surface of the sensing material. The reactive oxygen species lead to high resistance of the sensor. Superoxide O_2^- ion, monoatomic O^- ion, and peroxide species O^{2-} are three typical reactive oxygen species that are generally proposed as intermediates in the O_2 activation and dissociation process: $O_2 \rightarrow O_2^- \rightarrow O^- \rightarrow O^{2-}$.[47, 48] When the sensor

is exposed to an analyte gas (here ethanol), ethanol molecules are oxidized by surface-adsorbed reactive oxygen species (e.g., O_2^-, O^{2-}, O^-) to produce carbon dioxide and water on the In_2O_3 surface.[49] The oxidation reactions release more electrons into the crystal bulk, thus leading to low resistance of the sensor. Usually, a larger surface area leads to better gas sensing properties. However, the specific surface areas were measured to be 16.74 m^2 g^{-1} for In_2O_3 octodecahedra, 24.87 m^2 g^{-1} for In_2O_3 cubes and 36.75 m^2 g^{-1} for In_2O_3 particles, respectively. The results indicate that the enhanced gas sensing performance of In_2O_3 octodecahedra sensor is not attributed to the surface area but the type and arrangement of the atoms on the surface of the material.

Owing to the fact that the phase transformation from $In(OH)_3$ to In_2O_3 can introduce the oxygen vacancy, stoichiometric In_2O_3 is transformed into nonstoichiometric In_2O_{3-x} during the annealing process at high temperature. An n-type semiconductor oxide is formed because of the deficiency of oxygen.[28] The oxygen vacancy concentration of In_2O_3 sample could have important effect on the sensor sensitivity. In order to understand the defect state of the In_2O_3 product and investigate the relationship between oxygen vacancy and gas sensing performance, X-ray photoelectron spectroscopy (XPS) analysis was performed on the three different In_2O_3 samples. The In 3d core level spectra of the three In_2O_3 samples show two peaks located at 444.3 and 451.9 eV in Fig. 6b, which could be attributed to the characteristic spin-orbit split $3d_{5/2}$ and $3d_{3/2}$, respectively. Fig. 6a displays the O1s core level spectra of the three In_2O_3 products, and two peaks can be clearly identified from the spectra. One peak at 529.8 eV is deemed as the binding energy of O atoms in In-O-In bond corresponding to oxygen-sufficient state, in which In atoms are in full complement with their neighboring O atoms (crystal lattice oxygen). While the other located at 531.2 eV can be attributed to oxygen defects corresponding to oxygen-deficient state.[20, 50, 51] However, the ratios of oxygen-deficient area to oxygen-sufficient area for In_2O_3 octodecahedra, cubes and particles are 1.17, 1.05 and 1.02, respectively (Fig. 6a). We can conclude that the amounts of oxygen vacancy are more than that of crystal lattice O atoms. It can be also confirmed that there are more oxygen vacancies for In_2O_3 octodecahedra than In_2O_3 cubes and particles. Each oxygen vacancy offers two electrons and an active site for adsorption of oxygen species. The In_2O_3 octodecahedra sample should be with larger numbers of oxygen vacancies and electron donors, which is favorable for the formation of oxygen adsorbents.

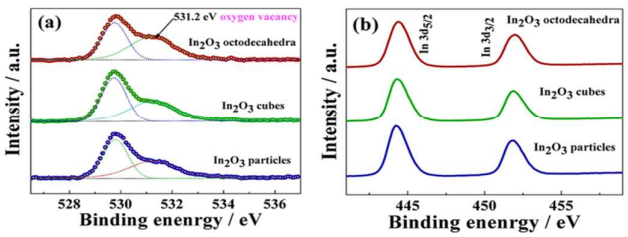

Fig. 6 (a) the O1s XPS spectra and (b) In 3d core level spectra for In_2O_3 octodecahedra, cubes and particles.

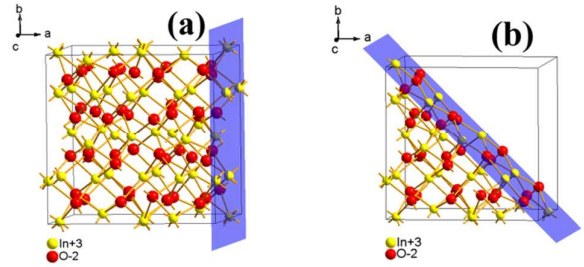

Fig. 7 Schematic models of perfect In_2O_3 crystal facets: (a) the (100) facet and (b) the (110) facet.

Due to the dissimilarity of atom arrangement at different crystal facets, the amount of oxygen vacancies would be inequality. In addition, the different reactivity and selectivity of sensing material depend greatly upon the different arrangement manner of surface atoms and the number of dangling bonds on different crystal planes, which is rely on the surface defect of different facets. The sequence of gas sensing performance among In_2O_3 octodecahedra, cubes and particles is octodecahedra > cubes > particles. It is worth mentioning that the surface area of In_2O_3 octodecahedra is the lowest. Therefore, crystal facets play an important role in the improvement of gas sensing properties and {110} facets have more important effect than {100} facets on gas sensing properties. Fig. 7 shows schematic models of In_2O_3 {100} and {110} facet, which consist of different surface atoms. As shown in Fig. 7a, b, the {110} facets are composed of In and O atoms, while the {100} facets only consist of In atoms. The above XPS results disclose that the conversion process of $In(OH)_3$ into In_2O_3 create a large number of oxygen vacancies on the In_2O_3 surfaces. The {110} facets are more easy to release O atoms to produce the oxygen vacancy than the {100} facets during the phase transformations process from $In(OH)_3$ to In_2O_3. This could be the reason that In_2O_3 octodecahedra with {110} facets have higher oxygen vacancy concentration than that of In_2O_3 cubes and particles. The presence of oxygen vacancies, particularly close to the In_2O_3 octodecahedra surface, increases the availability of the active adsorption sites for the oxygen species.

The enhanced gas sensing mechanism of In_2O_3 octodecahedra with {110} facets is interpreted by the resistance change originated from the chemisorbed oxygen species on the depletion surface layer as shown in Fig. 8. The high concentration of oxygen vacancy on {110} facets facilitates the adsorption of molecular oxygen and produces more reactive oxygen species, which increases the chance of In_2O_3 interacting with the analyte gases.[52] When In_2O_3 {110} facets is exposed to air, oxygen molecules would adsorb on the oxygen vacancy and form reactive oxygen species. The electrons are extracted from the conduction band and leads to a high resistance of In_2O_3 materials in air, as depicted in Fig. 8a. When the In_2O_3 {110} facets are exposed to an analyte gases reactive oxygen species on the In_2O_3 {110} facets, resulting in a low resistance of In_2O_3 materials because the

trapped electrons will be released back to the conduction band in this process.

Since less energy would be required to form oxygen vacancies on a facet with a higher surface energy,[53-55] the selective exposure of high energy facets would facilitate the formation of oxygen vacancies. This would improve the gas sensing properties. For In_2O_3 with a *bcc* structure, the surface energy relationships among the low-index facets should correspond to γ {111} < γ {100} < γ {110},[56-61] which determinesthat high energy {110} facet has a relatively high concentration of oxygen vacancy. The {110} facet has thus high activity for adsorption of reactive oxygen species (O_2^-, O^{2-}, O^-) and the analyte gas, which is in agreement with the XPS analysis. The discussion aforementioned demonstrates the mechanism for the high performance of the as-prepared In_2O_3 octodecahedra enclosed by {110} facets in comparison with In_2O_3 cubes and particles.

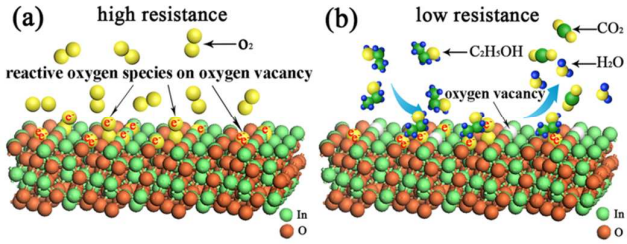

Fig. 8 Schematic representation of gas sensing mechanism on the In_2O_3 (110) facet: (a) high resistance in air and (b) low resistance in reducing gas.

Conclusions

In summary, In_2O_3 octodecahedra co-exposed with {110} and {100} facets were prepared by annealing the corresponding $In(OH)_3$ precursor. In_2O_3 cubes exposing {100} facets and irregular particles were also synthesized for comparison. The octodecahedral In_2O_3 sensor shows the best gas sensing performance compared with the cubic and particle In_2O_3 sensor. The enhanced gas sensing performance of In_2O_3 octodecahedra should be attributed to the high oxygen vacancies concentration of In_2O_3 octodecahedra and exposed high energy {110} facets. The results demonstrate that it is possible to improve gas sensing performance of In_2O_3-based sensors by the shape-controlling strategy. More importantly, the present study motivates us to further explore the preparation of other metal oxides with special crystal facet exposed, which has promising applications to other fields such as energy conversion and environmental protection.

Acknowledgements

This work was financially supported by projects of Natural Science Foundation of China (21271055, 21471040), the Fundamental Research Funds for the Central Universities (HIT. IBRSEM. A. 201410) and Open Project of State Key Laboratory of Urban Water Resource and Environment, Harbin Institute of Technology (QAK201304).

Notes and references

1 A. Seyed-Razavi, I. K. Snook and A. S. Barnard, *J. Mater. Chem.*, 2010, **20**, 416-421.
2 Z. L. Wang, *J. Phys. Chem. B*, 2000, **104**, 1153-1175.
3 T. K. Sau, A. L. Rogach, F. Jäckel, T. A. Klar and J. Feldmann, *Adv. Mater.*, 2010, **22**, 1805-1825.
4 G. Korotcenkov, *Mater. Sci. Eng. R*, 2008, **61**, 1-39.
5 X. Xu, D. Wang, J. Liu, P. Sun, Y. Guan, H. Zhang, Y. Sun, F. Liu, X. Liang, Y. Gao and G. Lu, *Sens. Actuators, B*, 2013, **185**, 32-38.
6 Z. Cheng, L. Song, X. Ren, Q. Zheng and J. Xu, *Sens. Actuators, B*, 2013, **176**, 258-263.
7 L. Gao, Z. Cheng, Q. Xiang, Y. Zhang and J. Xu, *Sens. Actuators, B*, 2015, **208**, 436-443.
8 H. Dong, Y. Liu, G. Li, X. Wang, D. Xu, Z. Chen, T. Zhang, J. Wang and L. Zhang, *Sens. Actuators, B*, 2013, **178**, 302-309.
9 G. Korotcenkov, S. D. Han, B. K. Cho and V. Brinzari, *Crit. Rev. Solid State*, 2009, **34**, 1-17.
10 N. Yamazoe, G. Sakai and K. Shimanoe, *Catal. Surv. Asia*, 2003, **7**, 63-75.
11 A. Gurlo, M. Ivanovskaya, N. Bârsan, M. Schweizer-Berberich, U. Weimar, W. Göpel and A. Diéguez, *Sens. Actuators, B*, 1997, **44**, 327-333.
12 G. Korotcenkov and B. K. Cho, *Prog. Cryst. Growth Ch.*, 2012, **58**, 167-208.
13 G. Korotcenkov and B. K. Cho, *Sens. Actuators, B*, 2011, **156**, 527-538.
14 G. Korotcenkov, V. Brinzari, M. Ivanov, A. Cerneavschi, J. Rodriguez, A. Cirera, A. Cornet and J. Morante, *Thin Solid Films*, 2005, **479**, 38-51.
15 M. Batzill, *Sensors*, 2006, **6**, 1345-1366.
16 X. Han, M. Jin, S. Xie, Q. Kuang, Z. Jiang, Y. Jiang, Z. Xie and L. Zheng, *Angew. Chem., Int. Ed.*, 2009, **48**, 9180-9183.
17 X. Wang, X. Han, S. Xie, Q. Kuang, Y. Jiang, S. Zhang, X. Mu, G. Chen, Z. Xie and L. Zheng, *Chem. Eur. J.*, 2012, **18**, 2283-2289.
18 M. R. Alenezi, A. S. Alshammari, K. D. G. I. Jayawardena, M. J. Beliatis, S. J. Henley and S. R. P. Silva, *J. Phys. Chem. C*, 2013, **117**, 17850-17858.
19 J. Liu, X. L. Chen, W. J. Wang, Y. Liu, Q. S. Huang and Z. P. Guo, *CrystEngComm*, 2011, **13**, 3425-3431.
20 Y. Liu, C. Kong, X. Lü, F. Liao, F. Huang and J. Lin, *Cryst. Growth Des.*, 2012, **12**, 4104-4108.
21 B. Geng, C. Fang, F. Zhan and N. Yu, *Small*, 2008, **4**, 1337-1343.
22 A. Shanmugasundaram, B. Ramireddy, P. Basak, S. V. Manorama and S. Srinath, *J. Phys. Chem. C*, 2014, **118**, 6909-6921.
23 Z. Zhuang, Q. Peng, J. Liu, X. Wang and Y. Li, *Inorg. Chem.*, 2007, **46**, 5179-5187.
24 Q. Liu, W. Lu, A. Ma, J. Tang, J. Lin and J. Fang, *J. Am. Chem. Soc.*, 2005, **127**, 5276-5277.
25 C. H. Liang, G. W. Meng, Y. Lei, F. Phillipp and L. D. Zhang, *Adv. Mater.*, 2001, **13**, 1330-1333.
26 Z. W. Pan, Z. R. Dai and Z. L. Wang, *Science*, 2001, **291**, 1947-1949.
27 H. Yang, Q. Shi, B. Tian, Q. Lu, F. Gao, S. Xie, J. Fan, C. Yu, B. Tu and D. Zhao, *J. Am. Chem. Soc.*, 2003, **125**, 4724-4725.
28 N. Du, H. Zhang, B. D. Chen, X. Y. Ma, Z. H. Liu, J. B. Wu and D. R. Yang, *Adv. Mater.*, 2007, **19**, 1641-1645.
29 H. Dong, Z. Chen, L. Sun, L. Zhou, Y. Ling, C. Yu, H. H. Tan, C. Jagadish and X. Shen, *J. Phys. Chem. C*, 2009, **113**, 10511-10516.

30 H. Yang, R. Zhang, H. Dong, J. Yu, W. Yang and D. Chen, *Cryst. Growth Des.*, 2008, **8**, 3154-3159.
31 B. Li, Y. Xie, M. Jing, G. Rong, Y. Tang and G. Zhang, *Langmuir*, 2006, **22**, 9380-9385.
32 J. Yang, C. Lin, Z. Wang and J. Lin, *Inorg. Chem.*, 2006, **45**, 8973-8979.
33 J. Liu, T. Luo, F. Meng, K. Qian, Y. Wan and J. Liu, *J. Phys. Chem. C*, 2010, **114**, 4887-4894.
34 W. J. Kim, D. Pradhan and Y. Sohn, *J. Mater. Chem*. *A*, 2013, **1**, 10193-10202.
35 X. Wang, M. Zhang, J. Liu, T. Luo and Y. Qian, *Sens. Actuators, B*, 2009, **137**, 103-110.
36 S. Tang, J. Zhang, S. Wu, C. Hu, Y. Li, L. Jiang and Q. Cui, *J. Phy. Chem. C*, 2014, **118**, 21170-21176.
37 M. Sun, S. Xiong, X. Wu, C. He, T. Li and P. K. Chu, *Adv. Mater.*, 2013, **25**, 2035-2039.
38 M. Meng, X. Wu, X. Zhu, L. Yang, Z. Gan, X. Zhu, L. Liu and P. K. Chu, *J. Phys. Chem. Lett.*, 2014, **5**, 4298-4304.
39 D. Seo, J. C. Park and H. Song, *J. Am. Chem. Soc.*, 2006, **128**, 14863-14870.
40 G. H. Jeong, M. Kim, Y. W. Lee, W. Choi, W. T. Oh, Q. H. Park and S. W. Han, *J. Am. Chem. Soc.*, 2009, **131**, 1672-1673.
41 Y.-X. Chen, S.-P. Chen, Z.-Y. Zhou, N. Tian, Y.-X. Jiang, S.-G. Sun, Y. Ding and Z. L. Wang, *J. Am. Chem. Soc.*, 2009, **131**, 10860-10862.
42 M. Leng, M. Z. Liu, Y. B. Zhang, Z. Q. Wang, C. Yu, X. G. Yang, H. J. Zhang and C. Wang, *J. Am. Chem. Soc.*, 2010, **132**, 17084-17087.
43 H. L. Cao, X. F. Qian, C. Wang, X. D. Ma, J. Yin and Z. K. Zhu, *J. Am. Chem. Soc.*, 2005, **127**, 16024-16025.
44 Y. Zhang, B. Deng, T. Zhang, D. Gao and A.-W. Xu, *J. Phys. Chem. C*, 2010, **114**, 5073-5079.
45 A. Kolmakov and M. Moskovits, *Annu. Rev. Mater. Res.*, 2004, **34**, 151-180.
46 G. Korotcenkov, *Mater. Sci. Eng. B*, 2007, **139**, 1-23.
47 G. I. Panov, K. A. Dubkov and E. V. Starokon, *Catal. Today*, 2006, **117**, 148-155.
48 N. Yamazoe, J. Fuchigami, M. Kishikawa and T. Seiyama, *Surf. Sci.*, 1979, **86**, 335-344.
49 X. Xu, H. Fan, Y. Liu, L. Wang and T. Zhang, *Sens. Actuators, B*, 2011, **160**, 713-719.
50 F. Lei, Y. Sun, K. Liu, S. Gao, L. Liang, B. Pan and Y. Xie, *J. Am. Chem. Soc.*, 2014, **136**, 6826-6829.
51 J. Gan, X. Lu, J. Wu, S. Xie, T. Zhai, M. Yu, Z. Zhang, Y. Mao, S. C. I. Wang, Y. Shen and Y. Tong, *Sci. Rep.*, 2013, **3**.
52 A. Yu, J. Qian, H. Pan, Y. Cui, M. Xu, L. Tu, Q. Chai and X. Zhou, *Sens. Actuators, B*, 2011, **158**, 9-16.
53 T. Désaunay, G. Bonura, V. Chiodo, S. Freni, J. P. Couzinié, J. Bourgon, A. Ringuedé, F. Labat, C. Adamo and M. Cassir, *J. Catal.*, 2013, **297**, 193-201.
54 J. Goclon, R. Grybos, M. Witko and J. Hafner, *Phys. Rev. B*, 2009, **79**, 075439.
55 W. Huang and Y. Gao, *Catal. Sci. Technol.*, 2014, **4**, 3772-3784.
56 C. Dewei, Z. Yu-Ping, J. Dongliang and X. Jiaqiang, *Nanotechnology*, 2007, **18**, 435605.
57 Y.-G. Yan, Y. Zhang, H.-B. Zeng and L.-D. Zhang, *Cryst. Growth Des.*, 2007, **7**, 940-943.
58 M. Kumar, V. N. Singh, B. R. Mehta and J. P. Singh, *J. Phys. Chem. C*, 2012, **116**, 5450-5455.
59 G. Cheng, E. Stern, S. Guthrie, M. A. Reed, R. Klie, Y. F. Hao, G. Meng and L. Zhang, *Appl. Phys. A*, 2006, **85**, 233-240.
60 M. Hafeez, T. Zhai, A. S. Bhatti, Y. Bando and D. Golberg, *Cryst. Growth Des.*, 2012, **12**, 4935-4943.
61 C.-H. Ho, C.-H. Chan, L.-C. Tien and Y.-S. Huang, *J. Phys. Chem. C*, 2011, **115**, 25088-25096.